

Particle image velocimetry measurements of a thermally convective supercritical fluid

Valori, Valentina; Elsinga, Gerrit E.; Rohde, Martin; Westerweel, Jerry; van der Hagen, Tim H.J.J.

DOI

[10.1007/s00348-019-2789-z](https://doi.org/10.1007/s00348-019-2789-z)

Publication date

2019

Document Version

Final published version

Published in

Experiments in Fluids

Citation (APA)

Valori, V., Elsinga, G. E., Rohde, M., Westerweel, J., & van der Hagen, T. H. J. J. (2019). Particle image velocimetry measurements of a thermally convective supercritical fluid. *Experiments in Fluids*, 60(9), Article 143. <https://doi.org/10.1007/s00348-019-2789-z>

Important note

To cite this publication, please use the final published version (if applicable). Please check the document version above.

Copyright

Other than for strictly personal use, it is not permitted to download, forward or distribute the text or part of it, without the consent of the author(s) and/or copyright holder(s), unless the work is under an open content license such as Creative Commons.

Takedown policy

Please contact us and provide details if you believe this document breaches copyrights. We will remove access to the work immediately and investigate your claim.

Green Open Access added to TU Delft Institutional Repository

'You share, we take care!' – Taverne project

<https://www.openaccess.nl/en/you-share-we-take-care>

Otherwise as indicated in the copyright section: the publisher is the copyright holder of this work and the author uses the Dutch legislation to make this work public.



Particle image velocimetry measurements of a thermally convective supercritical fluid

Valentina Valori^{1,2,3} · Gerrit E. Elsinga² · Martin Rohde¹ · Jerry Westerweel² · Tim H. J. J. van der Hagen¹

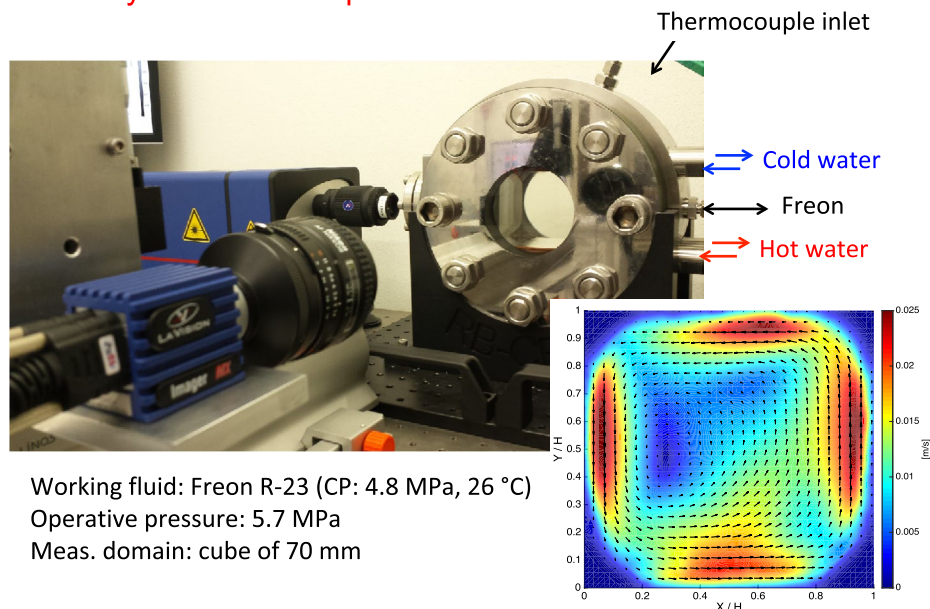
Received: 22 January 2019 / Revised: 30 May 2019 / Accepted: 3 August 2019
© Springer-Verlag GmbH Germany, part of Springer Nature 2019

Abstract

The feasibility of particle image velocimetry (PIV) in a thermally convective supercritical fluid was investigated. Hereto a Rayleigh–Bénard convection flow was studied at pressure and temperature above their critical values. The working fluid chosen was trifluoromethane because of its experimentally accessible critical point. The experiments were characterized by strong differences in the fluid density from the bottom to the top of the cell, where the maximum relative density difference was between 17 and 42%. These strong density changes required a careful selection of tracer particles and introduced optical distortions associated with strong refractive index changes. A preliminary background oriented schlieren (BOS) study confirmed that the tracer particles remained visible despite significant local blurring. BOS also allowed estimating the velocity error associated with optical distortions in the PIV measurements. Then, the instantaneous velocity and time-averaged velocity distributions were measured in the mid plane of the cubical cell. Main difficulties were due to blurring and optical distortions in the boundary layer and thermal plumes regions. An *a posteriori* estimation of the PIV measurement uncertainty was done with the statistical correlation method proposed by Wieneke (Measure Sci Technol 26:074002, 2015). It allowed to conclude that the velocity values were reliably measured in about 75% of the domain.

Graphic abstract

PIV and BOS measurements of a thermally convective supercritical fluid



Extended author information available on the last page of the article

1 Introduction

Supercritical (SC) fluids are very interesting for energy production, where they are mainly used as cooling fluids (see, e.g., Pioro and Kirillov 2013). The thermodynamic efficiency of a power plant can be significantly increased by extending its cooling cycle to temperatures in the SC region (Pioro and Kirillov 2013; Pioro 2012; Schuster et al. 2010; Karellas and Schuster 2008; Feher 1968). Research is going on to design a new kind of nuclear reactor cooled by supercritical water, i.e., the supercritical water reactor (SCWR), for the fourth generation of nuclear reactors (International Forum 2017; Pioro and Romney 2016; Buongiorno and MacDonald 2003; Oka and Koshizuka 1993). One of the main current open challenges for the development of this kind of reactor is related to the validation of heat transfer models at SC conditions. At SC conditions, fluids experience a sharp change of material properties, and as a result, their heat transfer behavior is very different with respect to sub-critical conditions (Yoo 2013). Experimental studies were performed in SC fluids with wall and bulk temperatures, heat fluxes, and mass flow rates as measured quantities (Huang et al. 2016; Jackson 2006, 2013; Jiang et al. 2006; Pioro et al. 2004). Local velocity measurements at SC conditions were done by Kurganov and Kaptil'ny (1992). This study showed velocity profiles in a pipe measured by Pitot tubes inserted in the flow. Vukoslavčević et al. (2005) performed local simultaneous velocity and temperature measurements, using hot and cold-wire probes, in supercritical CO₂. Furthermore, two previous velocity studies using single-point optical measurement techniques (i.e., laser Doppler velocimetry) near or above the critical point do exist, but for very particular conditions. In the study by Ashkenazi and Steinberg (1999), the temperature difference between the two horizontal plates of their thermal convection system was kept within a few mK, to maintain Boussinesq conditions for the working fluid (Boussinesq 1903). In another study, performed by Licht et al. (2009), the measurements were done in a square annulus, and forced and mixed convection conditions were studied, with water as working fluid, with bulk temperatures of 175–400 °C with upward mass fluxes of 300 kg/(m² s) and 1000 kg/(m² s) and heat fluxes of 0, 200, and 440 kW/m², at a pressure of 25 MPa.

To the knowledge of the authors, velocity field measurements by PIV at SC conditions have never been done previously. In this paper, the applicability of the PIV technique to supercritical fluids is studied. The very strong changes in fluid properties occurring at these conditions make it challenging to perform PIV measurements for several reasons. One is that due to the strong density variations within the flow domain, the tracer particles may not

be able to follow the flow or may not remain suspended in the flow at all. Because of density changes, also the number of the particles within the measurement domain may not be sufficiently high or uniform as desired for PIV measurements. Other reasons are related to the gradients in refractive index, which can cause particle image blur and introduce errors in the measured position of the particles and their velocity, as shown by Elsinga et al. (2005). In their study, a method was developed to quantify and correct for such errors in 2D compressible flows with a stationary and smoothly varying density distribution. They further showed that the second derivative of the refractive index in the direction of the velocity is the major source of velocity errors. PIV studies in fluids with strong localized changes in the refractive index were performed in compressible flows by Murphy and Adrian (2010) and by Elsinga and Orlicz (2015). Murphy and Adrian (2010) developed a high speed PIV system to study blast waves. Elsinga and Orlicz (2015) performed particle tracking velocimetry (PTV) and PIV measurements together with light-ray tracing predictions and found that optical errors in the velocity measurements of shock waves strongly depend on the angle between the viewing direction and the plane of the shock. These insights and methods were originally developed for compressible flows, but apply equally to thermal convective flows at supercritical conditions. However, the changes in refractive index are much stronger and more three-dimensional in the latter case, which warrants a further assessment of the optical distortions as proposed here.

The present assessment is based on PIV measurements in a Rayleigh–Bénard (RB) convection cell operated at pressures and temperatures above the critical point. In addition, separate BOS measurements are taken to independently examine the optical distortion and estimate the associated errors in the PIV measurements. The cell and measurement setups are introduced in Sect. 2. As explained above, the selection of tracer particles is critical and will be deliberated in Sect. 2.2. Results from the BOS optical distortions study (Sect. 3) allow us to determine blur and estimate the position and velocity errors in PIV. After that, the PIV results at supercritical fluid conditions are presented (Sect. 4), and an estimation of the statistical measurement uncertainty is made (Sect. 4.3). In addition, we compare results at supercritical conditions with earlier experimental studies under non-Boussinesq (but sub-critical) conditions (Valori et al. 2017), and observe some distinct differences. Finally, a general method to estimate the uncertainty of the PIV cross-correlation algorithm (Wieneke 2015) is applied to the unconventional conditions of a supercritical fluid.

2 Experimental setup and experimental programme

The high-pressure RB cell is composed of a cube with two horizontal copper plates and four glass lateral walls. This cube is inserted inside a stainless-steel cylinder with three sight-glass flanges made of borosilicate to allow optical access to the flow. A drawing of the RB cell is shown in Fig. 1. The dimension of the internal cube is 70 mm in each direction. Two glass lateral walls of the RB cell (indicated in Fig. 1) are made of a special borosilicate for high-pressure applications (METAGLAS[®] Sight Glass Flange, Connection to DIN 2501-Type 11). Inside each horizontal copper plate, a duct for water was made. These two ducts are included in two low-pressure water circuits and provide the heat exchange to the RB cell. The flow rate of the water in the cooling and heating circuit was chosen to keep the difference in water temperature between entering and leaving the plate, within 0.6 K, being of the order of the uncertainty range of the thermocouples. For insulation purposes, the copper plates are not in direct contact with the stainless steel, but there is a gap between them, as shown in Fig. 1. This gap is filled with an insulator material, which is polyetheretherketone (DIN-abbreviation: PEEK).

The working fluid used is trifluoromethane (molecular formula: CHF₃, ASHRAE Number: R-23; American Society of Heating and Engineers 2017). It was chosen because of its experimentally accessible critical point (i.e., 48 bars or 4.8 MPa, at about 26 °C or about 299 K, Lemmon et al. 2013).

Table 1 summarizes the operative range of the RB high-pressure setup. More details about the facility can be found in the Ph.D. thesis of Valori (2018).

2.1 Pressure and temperature measurements

The pressure in the cell is measured by a PTX 510 Industrial Pressure Transmitter, with a range from 1.5 to 10,000 psi (0.1 to 68.9 MPa) and with an accuracy of $\pm 0.15\%$ in the full scale. At the pressure of the experiments, i.e., about 60 bar, the maximum uncertainty in the pressure value is 0.09 bar. The sensor is located in the feeding pipe of the cell indicated in Fig. 1.

One thermocouple each is located in either copper plate of the RB cell, as shown in Fig. 1. This is the reference thermocouple used in the experiments to indicate the absolute temperature of the plates. For each water circuit, there are two additional thermocouples immersed in the cooling/heating water circuit, i.e., at the inlet and at the outlet of the copper plates of the RB cell, respectively. In addition, there are thermocouples recording the temperature inside the reservoir tanks from which the cooling/heating water is pumped. The thermocouples used are LABFACILITY type

K, class 2, mineral insulated sensors. They were calibrated against two temperatures (triple point, 0 °C, and boiling water, 100 °C at standard atmospheric pressure) and have a maximum tolerance of ± 0.3 K.

2.2 Instrumentation for PIV and BOS measurements

Figure 2 presents the layout of the PIV system. The different components are discussed in more detail next.

Particles When selecting tracer particles for the experiments at supercritical conditions, we first need to look for appropriate mechanical particle properties allowing them to follow the fluid motion accurately. The difference between the fluid velocity, u , and the particle velocity, u_p , is known as slip velocity, u_{slip} . For very low particle Reynolds numbers (< 1 based on the particle diameter and the slip velocity), the slip velocity of a particle in a continuously accelerating fluid can be calculated using the Stokes drag law as (Raffel et al. 2007)

$$u_{\text{slip}} = u_p - u = d_p^2 \frac{(\rho_p - \rho)}{18\mu} a, \quad (1)$$

where d is the particle diameter, ρ_p is the density of the particle, ρ and μ are the density and the dynamic viscosity of the fluid, respectively, and a is the acceleration of the fluid.

At higher flow velocities the velocity-slip equation is more complex; see Adrian and Westerweel (2011), Raffel et al. (2007), Melling (1997), Mei (1996, 1994), and

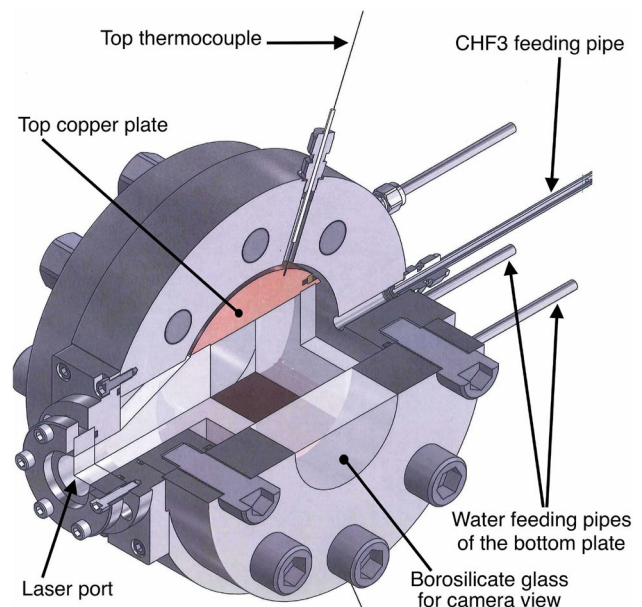


Fig. 1 Drawing of the Rayleigh–Bénard high-pressure convection cell, with indications of: copper plates, thermocouples, laser port, borosilicate glass wall, water feeding pipes, and CHF3 feeding pipe

Table 1 Operational conditions of the Rayleigh–Bénard facility

P_{\max} [bar]	P_{\min} [bar]	T_{\max} [°C]	T_{\min} [°C]
60	0.1	70	20

T_{\max} and T_{\min} are the maximum and minimum temperatures that can be reached in the copper plates of the cell, while P_{\max} and P_{\min} are the maximum and minimum operational pressures of the facility

also other aspects, like added mass and unsteady history (Mei 1996) should be taken into account in the choice of appropriate tracers particles. Their effect was studied by Mei (1996) with a frequency response analysis of the particle to a sinusoidal oscillation of the free stream. In this study, the frequency response of the particle was expressed as a function of a Stokes number, defined as the non-dimensional frequency of the fluid oscillation, and the ratio of the particle and the fluid densities. For a density ratio between particle and fluid between 0.56 and 1.62 a frequency response with a cutoff of 1/2 or 2, of the tracer particles was found (Mei 1996). On the basis of the particle-frequency response, a range of particle to fluid density ratio between 0.56 and 1.62 is required for the PIV tracer particles (Adrian and Westerweel 2011).

The present experiments were characterized by a substantial variation of the fluid density and viscosity within the cell (see Table 3). For each experimental condition, tracer particles were selected taking into account the density of the fluid at the average temperature in the cell, T_m , given by the arithmetic average between bottom plate temperature, T_b , and top plate temperature, T_t , as well as the fluid densities at the top and bottom plate temperatures. The former was considered to minimize the velocity slip due to gravity, and the latter to make sure that the largest and smallest density ratio of the experiments was within the limits of good particle-frequency response as reported by Mei (1996). Table 2 reports the density and the diameter of the particles used in the present experiments, the ratio between a characteristic time due to Stokes drag and the integral time scale of the flow, the ratio between the slip velocity due to gravity only, and the large-scale circulation velocity of the flow, and the ratio between the particle density and the fluid density. The density ratios are between 0.89 and 1.61, complying with the criteria proposed by Mei (1996) for good tracer properties, which is particle to fluid density ratio between 0.56 and 1.62. The particles used are hollow glass microspheres, produced by Cospheric LLC. They are made of sodium silicate (77–88 % in weight), sodium borate (7–18 % in weight), and amorphous silicon dioxide (< 5% in weight). Particles of these materials were selected, because they are chemically compatible with the supercritical trifluoromethane (R-23) used in the experiments. Since the particles showed

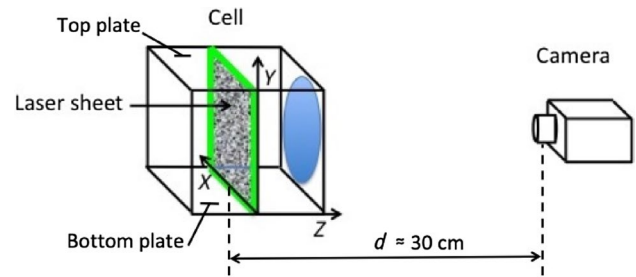


Fig. 2 Sketch of the relative position of camera, cell, and laser sheet for planar PIV measurements, with indication of X, Y, and Z coordinates. The experimental parameters of the measurements are reported in Table 2

the tendency to agglomerate in static clusters, of about 1 cm of length, it was necessary to prevent cluster formation before starting the operation of the facility. A solution was found by cleaning the particles with ethanol before introducing them into the setup. Ethanol dissolves and removes chemicals that may be attached to the particles. In addition, the internal walls of the setup were cleaned with ethanol to avoid adhesion of the glass particles to the surfaces. Figure 3 presents a close-up of a camera recording showing the particle images acquired in the present RB flow at supercritical conditions.

Laser The light source used in the measurements is a diode pumped solid-state laser. It is a continuous wave laser with a power of 5 W at a wavelength of 532 nm. A spherical and a cylindrical lens were used to generate a laser sheet. The cylindrical lens had a focal length of -3.9 mm. This small focal length was necessary to create a laser sheet that spanned the full height of the cell ($H=70$ mm) through the small lateral window of the cell (see Fig. 1). The laser sheet was located in the mid plane of the cell, and was about 1 mm thick (measured value).

Camera The camera used for the PIV measurements was a LaVision Imager MX, with a digital resolution of 2048×2048 pixels and a pixel pitch of $5.5 \mu\text{m}$. The image sensor was a CMOSIS CMV4000 with dimensions of 11.26×11.26 mm. The images were acquired at a frame rate of 3 Hz with an interframe time of $20 \mu\text{s}$, which corresponded to a maximum particle image displacement of 10–12 pixels. The camera was equipped with a lens with a focal length of 50 mm (Nikon model Nikkor AF f/1.4D) and the aperture stop used for the measurements was either 8 or 5.6, depending on the experiment (see Table 2). The field of view of the recordings was $7 \times 7 \text{ cm}^2$ resulting in an image magnification factor $M_0 = 0.13$. The depth of field (δ_z) of the measurements computed from Eq. (2):

$$\delta_z \cong 4 \left(1 + \frac{1}{M_0} \right)^2 f_{\#}^2 \lambda \quad (2)$$

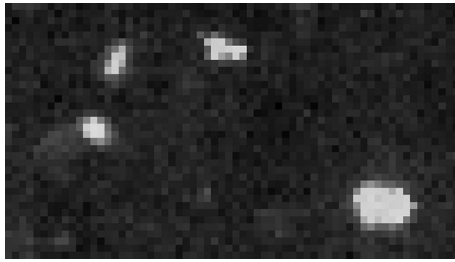


Fig. 3 Camera image of particles at supercritical conditions in a thermally convective flow (pressure: 5.52 MPa, temperature bottom plate: 309.5 K, temperature top plate: 307 K, fluid: F₃CH). The particles that are illuminated by the laser are visible as bright spots. The dimensions of the image are: 1.6 mm × 2.7 mm

Table 2 Experimental parameters for the PIV measurements: Aperture stop, $f_{\#}$, values of the experiments PIV SC_{liquid}, PIV SC_{max Δρ}, and PIV SC_{gas}

	PIV SC _{liquid}	PIV SC _{max Δρ}	PIV SC _{gas}
$f_{\#}$	8	5.6	5.6
ρ_p [g/cm ³]	0.68	0.55	0.55
d_p [μm]	5–20	5–27	5–27
$u_{\text{slip}}/(a\tau_l)$	0.3×10^{-4}	1.5×10^{-4}	3.5×10^{-4}
$u_{\text{slip-g}}/U_{\text{LSC}} \times 100$	0.8	4	0.9
$[\rho_p/\rho]$ min	0.89	0.93	1.35
$[\rho_p/\rho]$ max	1.05	1.32	1.61

ρ_p is the density of the particles, and d_p the particle diameter. $u_{\text{slip}}/(a\tau_l)$ is the ratio between the particle response time as computed by Eq. (1) (with density, ρ , and dynamic viscosity, μ , taken from CoolProp by Bell et al. (2014) at the average top–bottom temperature, T_m , of the cell) and an integral time scale of the flow estimated from experiments, τ_l . $u_{\text{slip-g}}/U_{\text{LSC}}$ represents u_{slip} computed as in Eq. 1 when the acceleration of the fluid is equal to the gravity acceleration, normalized by the large scale circulation velocity of the flow estimated from experiments, U_{LSC} . The last two rows show, respectively, the minimum and the maximum values of the ratio between the particle density, ρ_p , and the fluid density, ρ , for each PIV experiment (values of ρ at the top and the bottom temperatures of the cell at the pressures of the experiments were taken from the CoolProp database by Bell et al. (2014)

was about 5–10 mm depending on the $f_{\#}$. Hence, the laser-sheet thickness was smaller than the focal depth thickness ensuring good focusing conditions of the particles. The use of an $f_{\#}$ larger than necessary aids in maintaining a good focusing of the particles due to variations in refractive index that tend to blur the images when a smaller $f_{\#}$ is used.

The setup used for the BOS measurements (Richard and Raffel 2001) is similar to the one for the PIV measurements, with one main difference: The camera records images of a computer generated background dot pattern placed behind the cell, instead of the particles in the mid plane of the cell. The refractive index variation within the cell distorts the images of the background pattern (Richard

and Raffel 2001), which is measured using a cross-correlation algorithm similar to PIV.

2.3 Experimental programme

BOS measurements were performed at supercritical conditions to check the applicability of PIV in a region with strong optical distortions. Three experiments were done by varying the density difference between the top and the bottom of the cell. Afterwards, PIV measurements were done at the same experimental conditions. Table 3 shows the experimental conditions of all BOS and PIV experiments.

In this table, in the first six lines, the pressure, p , and the temperatures of the top, T_t , and of the bottom plates of the cell, T_b , are reported, together with the standard deviations (std) of the electric signal from the thermistors. The seventh line reports the mean value between the top and the bottom wall temperatures. The three experimental conditions chosen for the PIV and the preliminary BOS study are called SC_{liquid}, SC_{max Δρ} and SC_{gas}. The experiment SC_{max Δρ} is the one with the largest difference in density and refractive index between the top and the bottom of the cell. The experiment SC_{liquid} is characterized by larger values of the density, closer to the liquid phase, while the experiment SC_{gas} by lower values, closer to the gas phase.

The calculated densities, ρ , refractive indices, n , thermal expansion coefficients, α , dynamic viscosities, μ , kinematic viscosity, ν , and Prandtl number, Pr , at the top and bottom plate temperatures of the cell are reported in the bottom part of Table 3, together with their relative top–bottom variations (Δ). All the fluid property values of CHF₃ were taken from the CoolProp database (Bell et al. 2014), except the refractive index values as a function of ρ , $n(\rho)$, which were taken from Avdeev et al. (2004), where a relative error in $\Delta n/n$ of $\approx 0.01\%$ is indicated. $n(\rho)$ is defined using the Lorentz-Lorenz Eq. (3), which relates density and refractive index of a substance as

$$\frac{n^2 - 1}{n^2 + 2} = A\rho, \tag{3}$$

where A is a material constant related to polarizability, which does not depend on temperature. The values of $(\rho_t - \rho_b)/\rho(T_b)$ and $(n(\rho_t) - n(\rho_b))/n(\rho(T_b))$ show the importance of the difference in density or refractive index between the top and the bottom of the cell with respect to its value at the bottom plate temperature (T_b).

2.4 Data acquisition and processing

The PIV and BOS images were processed with the DaVis 8 software from LaVision GmbH. A two passes cross-correlation algorithm with decreasing interrogation window size was used. The size of the final pass was 32 × 32 pixels for all BOS measurements and 48 × 48 pixels for the PIV

experiments, except for one case, that is PIV $SC_{\max \Delta\rho}$ (see Table 3), where it was 64×64 pixels, to get a larger number of valid vectors. The overlap of the interrogation windows was 50%. The spatial resolution for the BOS measurements was 1.35 mm (based on window size), while for the PIV measurements, it was 2 mm, except for the $SC_{\max \Delta\rho}$ case, where it was 2.7 mm.

3 Assessment of imaging conditions using BOS

The BOS technique (Richard and Raffel 2001) was used to quantify optical distortions due to refractive index changes in supercritical fluids. These distortions result in (particle)

image blur (Sect. 3.1) and apparent image displacement (Sects. 3.2 and 3.3).

3.1 Evaluation of particle image blur

Instantaneous BOS recordings, at the experimental conditions of $SC_{\max \Delta\rho}$, with and without temperature difference across the cell, are shown in Fig. 4a, b. The optical distortions due to temperature gradients are visible in panel (a) as a blurring in the background image that is not visible in the corresponding (b) panel.

In Fig. 4a, three red dots are indicated. Two of the dots (B) and (C) are located in blurred regions: one close to the bottom boundary layer and another one in a plume at the center of the cell. The third dot (labeled A) is in a region without optical distortions. From this figure, it can be seen that the white dots on the background are difficult to

Table 3 Overview of the experimental conditions for the BOS and PIV experiments

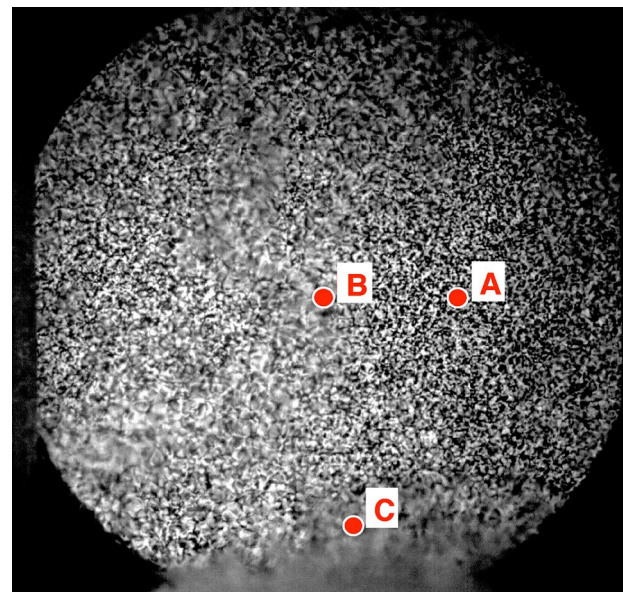
	BOS SC_{liquid}	BOS $\Delta T = 0$ SC_{liquid}	BOS $SC_{\text{max } \Delta\rho}$	BOS $\Delta T = 0$ $SC_{\text{max } \Delta\rho}$	BOS SC_{gas}	BOS $\Delta T = 0$ SC_{gas}	PIV SC_{liquid}	PIV $SC_{\text{max } \Delta\rho}$	PIV SC_{gas}
p [kPa]	5519	5390	5516.1	4318	5511.8	4585	5516.2	5499.5	5518.9
$\text{std}(p)$ [kPa]	6.10	2.35	4.25	2.7	4.94	2.94	6.93	3.18	6.37
T_t [K]	301.0	300.2	304.1	297.1	307.1	297.7	301.0	304.1	307.0
$\text{std}(T_t)$ [K]	0.07	0.07	0.08	0.07	0.08	0.08	0.08	0.08	0.08
T_b [K]	303.6	300	306.5	297.1	309.6	297.6	303.5	306.5	309.5
$\text{std}(T_b)$ [K]	0.07	0.07	0.08	0.07	0.08	0.07	0.07	0.08	0.08
T_m [K]	302.3	300.1	305.3	297.1	308.4	297.7	302.3	305.3	308.3
$\rho(T_t)$ [kg/m ³]	759.57	–	608.91	–	401.48	–	760.38	592.65	407.01
$\rho(T_b)$ [kg/m ³]	645.65	–	426.72	–	338.54	–	649.03	416.97	341.97
$\Delta\rho/\rho(T_b) \times 100$	17.64	–	42.69	–	18.59	–	17.16	42.13	19.02
$n(\rho(T_t))$	1.1134	–	1.0926	–	1.0589	–	1.1135	1.0901	1.0597
$n(\rho(T_b))$	1.0978	–	1.0633	–	1.0501	–	1.0963	1.0615	1.0506
$\Delta n/n(T_b) \times 100$	1.42	–	2.76	–	0.84	–	1.57	2.69	0.87
$\alpha(T_t)$ [K ⁻¹]	0.0395	–	0.1332	–	0.0916	–	0.0393	0.1470	0.0952
$\alpha(T_b)$ [K ⁻¹]	0.1053	–	0.1117	–	0.0489	–	0.1030	0.1058	0.0504
$\Delta\alpha/\alpha(T_b) \times 100$	–62.5	–	19.3	–	87.3	–	–61.8	38.9	88.9
$\mu(T_t)$ [μPa s]	52.01	–	38.26	–	25.71	–	52.09	37.04	25.97
$\mu(T_b)$ [μPa s]	41.19	–	26.91	–	23.1	–	41.47	26.43	23.23
$\Delta\mu/\mu(T_b) \times 100$	26.3	–	42.2	–	11.3	–	25.6	40.1	11.8
$\nu(T_t)$ [m ² /s]	0.0395	–	0.0233	–	0.0103	–	0.0396	0.0220	0.0106
$\nu(T_b)$ [m ² /s]	0.0266	–	0.0115	–	0.0078	–	0.0269	0.0110	0.0079
$\Delta\nu/\nu(T_b) \times 100$	48.5	–	103	–	32.1	–	47.2	100	34.2
$Pr(T_t)$	3.82	–	8.75	–	5.55	–	3.81	9.40	5.76
$Pr(T_b)$	7.39	–	6.68	–	3.20	–	7.27	6.35	3.28
$\Delta Pr/Pr(T_b) \times 100$	–48.3	–	31	–	73.4	–	–47.6	48.03	75.6

The working fluid is F₃CH. p is the pressure of the cell and $\text{std}(p)$ its standard deviation. T_t is the top plate temperature and $\text{std}(T_t)$ its standard deviation, T_b is the bottom plate temperature and $\text{std}(T_b)$ its standard deviation. T_m is the average top–bottom temperature, $T_m = (T_t + T_b)/2$. $\rho(T_t)$ [$n(\rho(T_t))$, $\alpha(T_t)$, $\mu(T_t)$, $\nu(T_t)$, $Pr(T_t)$] and $\rho(T_b)$ [$n(\rho(T_b))$, $\alpha(T_b)$, $\mu(T_b)$, $\nu(T_b)$, $Pr(T_b)$] are the fluid density [refractive index, isobaric thermal expansion coefficient, dynamic viscosity, kinematic viscosity, and Prandtl number] values at T_t and T_b , respectively, $\Delta\rho$ [Δn , $\Delta\alpha$, $\Delta\mu$, $\Delta\nu$, ΔPr] is the difference between $\rho(T_t)$ [$n(\rho(T_t))$, $\alpha(T_t)$, $\mu(T_t)$, $\nu(T_t)$, $Pr(T_t)$] and $\rho(T_b)$ [$n(\rho(T_b))$, $\alpha(T_b)$, $\mu(T_b)$, $\nu(T_b)$, $Pr(T_b)$]. ρ , α , μ , ν , and Pr values of F₃CH taken from the CoolProp database (Bell et al. 2014), and $n(\rho)$ values of F₃CH taken from Avdeev et al. (2004)

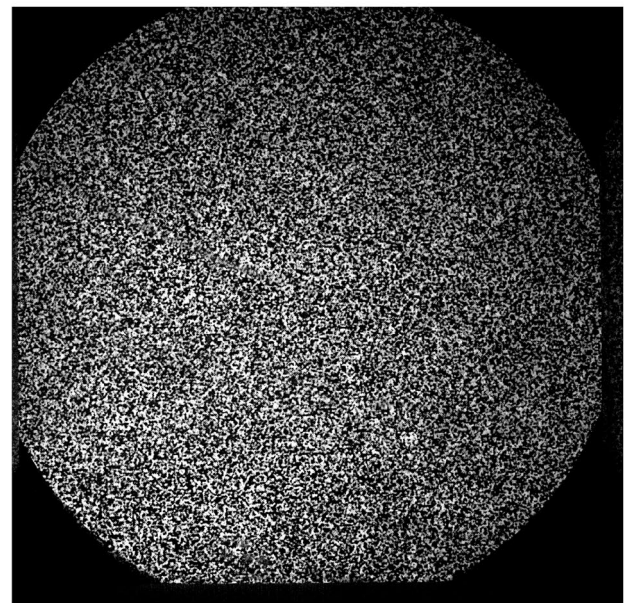
distinguish in the blurred regions. This can also happen with the images of tracer particles in the PIV measurements (even when the illuminated PIV particles are located at the cell half depth). Note that the thickness of the layer of fluid with refractive index changes in the PIV measurements is half the thickness for BOS measurements.

To quantify the blurring, the spatial autocorrelation function of the intensity was computed for each of the three locations marked by red dots in Fig. 4a, and compared to the case without temperature gradient. The intensity autocorrelation function (I_a) is based on the fluctuating intensity within a correlation window around the points. The size of the correlation window was chosen at 128×128 pixels, and it is the same size as the first-pass interrogation window used for the PIV measurements made at the same experimental conditions. Figure 5 shows the resulting normalized intensity autocorrelation peaks, I_a , for the case $SC_{\max \Delta \rho}$ (the condition with the largest refractive index changes). In absence of visible thermal plumes [panel (a)] no important decrease or broadening of the autocorrelation function peak is visible. A clear broadening of the peak is visible in the case with temperature difference across the cell, for the part in the bottom boundary layer [panel (c)], and for the plume [panel (b)]. This increase in peak width compared to the case at uniform temperature is a measure for image blur associated with temperature variations in the cell. Image blur also reduces contrast in the images resulting in an attenuation of the correlation peak magnitude, which is not apparent from Fig. 5 due to the chosen normalization. However, the reduced signal strength causes image noise to gain relative importance, which leads to a 'noise' spike at the origin, $\Delta x = 0$, in the intensity autocorrelation, most notably for the bottom boundary layer [panel (c) red line].

Based on the observed autocorrelation peak broadening, and assuming Gaussian blur, the blur diameter is estimated at 30 and 15 pixels for the bottom boundary layer and the plume, respectively. In PIV, since the laser sheet is at the cell half depth, the optical path through the refractive index field is reduced by half compared to BOS. According to Elsinga et al. (2005) the blur length scales with the cube of the optical path, which means that the expected blur diameter in the PIV imaging is less than 4 pixels for the present flow conditions. This implies that the PIV cross-correlation algorithm yields detectable peaks in most of the cell cross section even at this level of blur. The PIV measurement uncertainty associated with a 4-5 pixel particle image diameter is around 0.1 pixel for the cross-correlation window sizes used (Raffel et al. 2007; Adrian and Westerweel 2011). Therefore, particle image blur is not expected to significantly affect the overall accuracy of the PIV measurement.



(a)



(b)

Fig. 4 **a** Instantaneous camera image of the BOS background with temperature difference $\Delta T = 2.4$ K, at the experimental conditions of the case BOS $SC_{\max \Delta \rho}$. The three red dots with letters indicate the points, where the autocorrelation functions of Fig. 5 were calculated. **b** Camera image of the BOS background without temperature gradient, used as reference (BOS $\Delta T = 0$ $SC_{\max \Delta \rho}$ of Table 3). $\Delta T = 0$ K, $T_m = 297.1$ K, $p = 4318$ kPa

3.2 BOS time-average distortion

The average BOS displacement is due to the temperature dependency of the isobaric thermal expansion coefficient

of the fluid (see Table 3), and it contains two main effects. One is that the mean temperature of the reference recording without temperature gradient is different from the one with temperature gradient, and this leads to a different global magnification factor (M_0). The second effect is that in the cases with an imposed temperature gradient, the temperature field is not uniform throughout the measurement section, even when the time-averaged field is considered, and this leads to deflections of the light towards the lens.

To quantify these effects, the time-averaged BOS displacement was determined from 1-h long measurements with 10800 samples, which are the same measurement length and number of samples used in the PIV measurements for statistical reasons (see Sect. 4.2). The measured image displacements at the three experimental conditions are of the order of $10\mu\text{m}$. Considering the largest time-averaged BOS displacement, which was measured at the experimental conditions SC_{gas} , the global magnification M_0 does not change. This can be seen when comparing the maximum average displacement, being 7.3 pixels within the linear field of view of ≈ 2000 pixels (because $7 \ll 2000$). For PIV measurements this global magnification factor effect is even smaller and can be neglected, because the optical path through the fluid is only half as long with respect to the BOS measurements. Therefore, the mean optical displacement in the PIV images is estimated to be 1/4 of the displacement in the BOS images (Elsinga et al. 2005). However, the inhomogeneity of the instantaneous temperature field may lead to local deflections that are responsible for appreciable PIV velocity uncertainties, as shown next.

3.3 BOS instantaneous measurements

The instantaneous BOS displacement fluctuations highlights the instantaneous thermal structures of the flow. In all three cases these structures appear statistically uniformly distributed throughout the cell.

Local changes in the magnification factor due to the refractive index field are responsible for velocity errors in PIV measurements. In particular, it was shown that the relative velocity error is equal to the optical displacement gradient, ∇d , in the direction of the velocity vector, with a minor correction due to d itself (Elsinga et al. 2005). Examples of the displacement gradient, ∇d , measured by BOS are shown in Fig. 6, for the three experimental conditions. The maximum values of ∇d are of the order of 10%. Since ∇d , as computed from these measurements, corresponds to optical distortions that are integrated over the depth of the domain, and the flow is not two dimensional, it is not possible to directly correct the PIV measurements based on the present BOS measurements. However, the BOS results can be used to estimate an upper bound for the velocity error due to optical distortions. Consider a thermal structure located near the

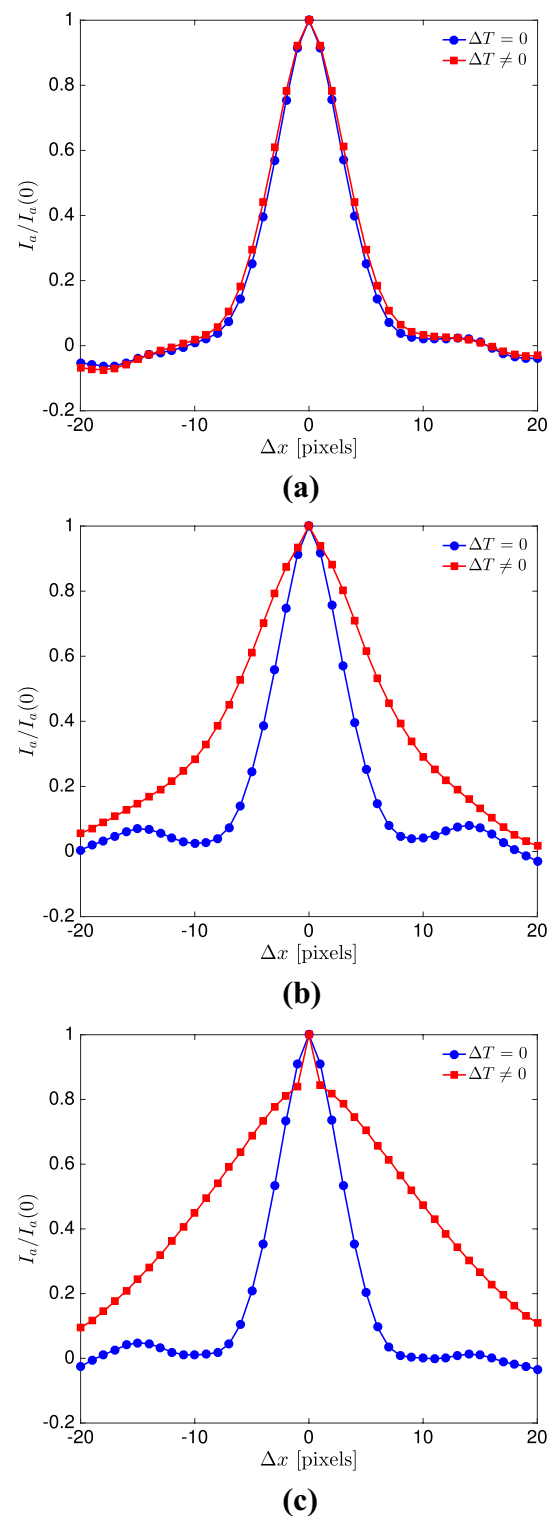


Fig. 5 Instantaneous autocorrelation functions in three points of the experiment $\text{SC}_{\text{max } \Delta\rho}$, with and without temperature difference ($\Delta T = 2.4\text{ K}$, squares and red line and $\Delta T = 0\text{ K}$, circles and blue line). The three points with A B C are indicated in Fig. 4a with red dots. **a** Point at the center of the cell, where no plumes are visually detectable, **b** point at the center of the cell, where a plume is visible, and **c** autocorrelation function in the point close to the bottom boundary layer

front window of the cell, which causes light to deflect with a certain angle. The corresponding distortion in the BOS or PIV image then is proportional to this angle multiplied with the distance between the thermal structure, i.e., front window, and the dot pattern (BOS), or the particles in the laser sheet (PIV). Because the distance is half for PIV, we expect the distortion d and ∇d to be halved for this thermal structure, which results in an upper bound of approximately 5% for the direct velocity error in the PIV measurements (Elsinga et al. 2005). Note that in thermal plumes and boundary layers the largest Δd is expected to misalign with the velocity, which would considerably reduce the errors.

4 PIV measurements

This section presents time-averaged velocity fields of all experiments as well as an instantaneous snapshot (Sect. 4.1), an assessment of the statistical uncertainty (Sect. 4.2), and an *a posteriori* estimation of the uncertainty with correlation statistics (Sect. 4.3).

4.1 Time-averaged and instantaneous velocity fields

Time-averaged velocity fields at the experimental conditions SC_{liquid} , $SC_{\text{max } \Delta\rho}$, and SC_{gas} are shown in Figs. 7, 8, and 9, respectively. No preprocessing of the raw images was performed, except for the experiment SC_{gas} , where a local time-averaged minimum image was subtracted from the camera recordings to reduce the noise. This was necessary to better distinguish the particles from the background. The presence of a large scale circulation flow, typical of RB convection (Ahlers et al. 2009), was observed in all experiments. The shape of the large scale circulation roll is very asymmetric in all the three cases. The experiment SC_{liquid} (Fig. 7) is the case with the largest magnitude of the integral velocity scale.

Since the flow direction was clockwise for the experiment SC_{liquid} and anti-clockwise for the other two cases, the SC_{liquid} flow fields (Figs. 7, 10, and 14) were mirrored with respect to the vertical axis to facilitate an easier comparison. The shape of the velocity field is very similar for the SC_{liquid} and $SC_{\text{max } \Delta\rho}$ cases (compare Figs. 7, 8). In particular, it is interesting to look at the asymmetry in the horizontal bottom jet of Figs. 7 and 8. In both cases at $X/H = 0.5$ the jet diverges going upwards with an inclination of about 45° in the large scale circulation direction. While the actual flow direction of the experiment of Fig. 7 is clockwise, and the figure was mirrored, the actual circulation direction of Fig. 8 is anti-clockwise. Hence, the observed circulation direction and the associated asymmetry cannot be explained by an asymmetry of the experimental setup.

In all three cases there are two distinctive low velocity regions. In the SC_{liquid} and $SC_{\text{max } \Delta\rho}$ cases (Figs. 7, 8) the two regions with low velocity values are approximately at $X/H \simeq 0.3$ and $Y/H \simeq 0.5$, and $X/H \simeq 0.5$ and $Y/H \simeq 0.7$, while in the SC_{gas} case (Fig. 9), they are approximately at $X/H \simeq 0.35$ and $Y/H \simeq 0.75$, and $X/H \simeq 0.75$ and $Y/H \simeq 0.75$. The presence of two low velocity regions in the time-averaged velocity fields suggests that the instantaneous large-scale-flow structure is probably more complex than just one big roll, as one can find under Boussinesq conditions. Moreover, strong asymmetries in the large-scale-flow are visible in all experiments, which can be explained by looking at the strong fluid property variations between top and bottom of the cell, as quantified in Table 3. In particular, the relative changes between the top and the bottom of the cell can be up to 100% for the kinematic viscosity in the experiment $SC_{\text{max } \Delta\rho}$, or $\pm 48\%$ for the values of the Prandtl number in the experiments SC_{liquid} and $SC_{\text{max } \Delta\rho}$. Asymmetries in the value of the large-scale circulation velocity between the top and at the bottom of the cell were observed in previous numerical and experimental studies under non-Boussinesq (but sub-critical) conditions in liquids (Horn et al. 2013; Horn and Shishkina 2014; Valori et al. 2017). In these studies it was found that the top–bottom velocity asymmetry was due to the top–bottom variation of the temperature dependent kinematic viscosity of the fluid. At the present experimental conditions, the flow physics is more complex, because not only the kinematic viscosity, but all the fluid properties are strongly temperature dependent (see Table 3) and it is not possible to isolate the effect of one of them from the others. All of them can interplay a role in the observed asymmetries of the mean velocity field.

Figure 10 shows an example of the instantaneous velocity field of the SC_{liquid} experiment. From this snapshot, several details of the flow can be observed: A thermal plume detaches from the bottom boundary layer, at $X/H \simeq 0.6$, and goes towards the top-right direction, carried by the large scale flow. Close to the right side wall, there are groups of ascending plumes, while at the left side wall, there is a group of descending plumes ($Y/H \simeq 0.5$ and about $0.01 < X/H < 0.15$). Plumes are visible also at the center of the cell. This picture is consistent with, and provides details about, its corresponding time-average velocity field shown in Fig. 7.

4.2 Statistical uncertainty

The statistical convergence of the measured average flow incorporates effects of both measurement noise and flow unsteadiness. RB flows are indeed characterized by a periodic large-scale circulation of the flow with large associated time scales. A sufficient number of statistically independent samples is necessary for an accurate measurement of the

Fig. 6 Magnitude of the adimensional spatial gradient (∇d) of an instantaneous BOS image displacement, after subtraction of its time-average image displacement, for the case BOS SC_{liquid} (a), BOS SC_{max Δρ} (b), and BOS SC_{gas} (c)

time-mean velocity (\bar{u}), from instantaneous velocity fields (u_i). The local statistical relative uncertainty on the mean velocity (δu) was estimated as

$$\delta u = \frac{\sigma_u}{\bar{u}\sqrt{n}}, \quad (4)$$

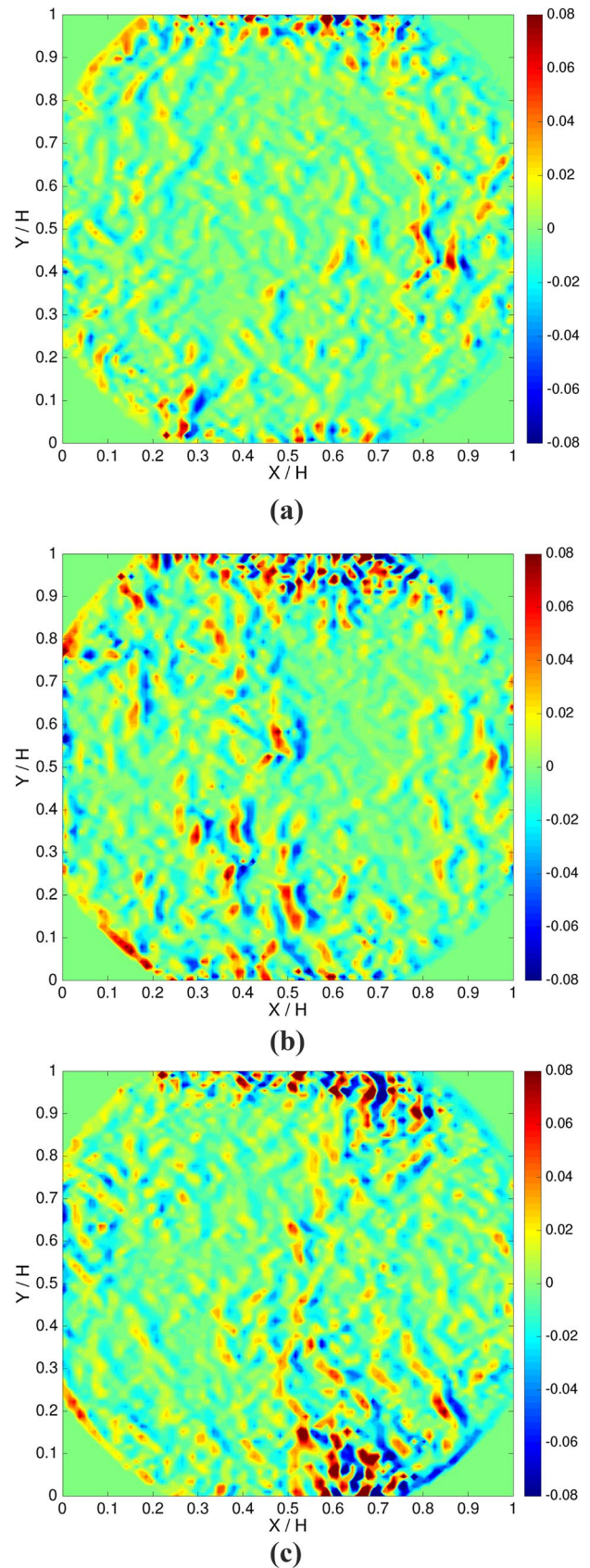
where σ_u is the standard deviation, and n is the number of uncorrelated samples, which is estimated by

$$n = \frac{N}{\tau \times f}, \quad (5)$$

with the number of samples $N = 10800$ acquired at the frequency of $f = 3$ Hz. Furthermore, τ represents the turnover time of the flow, based on the large scale circulation velocity U_{LSC} . The development of a large-scale-circulation roll is typical of RB convection, for a wide range of the non-dimensional controlling parameters, Rayleigh and Prandtl numbers, under Boussinesq conditions, and aspect ratio one geometries (Ahlers et al. 2009). The mean velocity of this roll can be used to characterize the extent of turbulence within the flow (Ahlers et al. 2009).

To obtain an estimate for U_{LSC} , we consider the spatially filtered velocity magnitude $|u|$ in the plume along the right side wall, i.e., at $X/H \simeq 0.9$ and $Y/H \simeq 0.5$. Spatial filtering is performed by averaging over 10×15 data points around the point of interest. Time correlations of the U_{LSC} fluctuations are shown for the cases SC_{liquid}, SC_{max Δρ}, and SC_{gas}, in Figs. 11, 12, and 13, respectively. Periodicity is found for the cases SC_{liquid} and SC_{max Δρ}, but not for the case SC_{gas}. This is probably due to two factors: longer characteristic times because of different values of the fluid properties, and to a complex 3D structure of the flow, which could not be captured at the position of the measurement section. The period τ thus obtained is 5.3, 6 and 10 seconds for the cases SC_{liquid}, SC_{max Δρ}, and SC_{gas}, respectively. Table 4 summarizes the values of the large-scale circulation velocity, U_{LSC} , in the three PIV experiments, its statistical uncertainty, $\delta u(\tau)$, its standard deviation, σ_u , and characteristic time, τ , which were used for the calculation of $\delta u(\tau)$.

It is important to point out that the observed asymmetries in the flow are not due to measurements errors. This can be seen by comparing the magnitude of the measured asymmetry to the statistical uncertainty. For example, for the experiment SC_{liquid}, the asymmetry in the velocity of the upward and the downward jet is of the order of 5 mm/s, which is 25 times larger than the corresponding statistical uncertainty (0.2 mm/s). Furthermore, optical distortions do



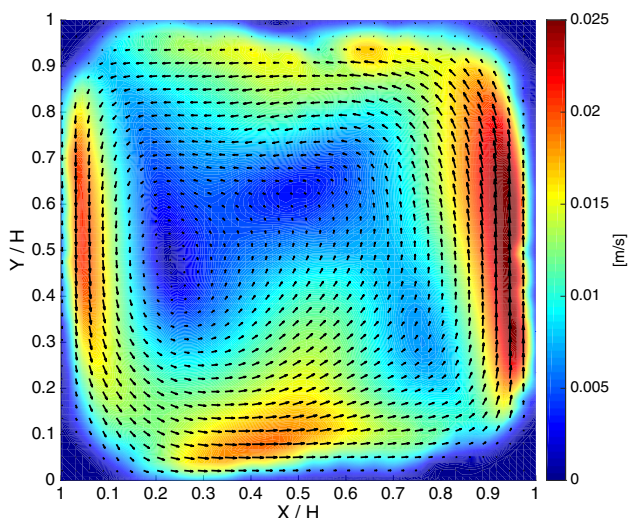


Fig. 7 Time-averaged velocity field of the PIV experiment SC_{liquid} . The color scale indicates the magnitude of the mean velocity \bar{u} , while the arrows show its direction. Only one arrow every four data points is plotted

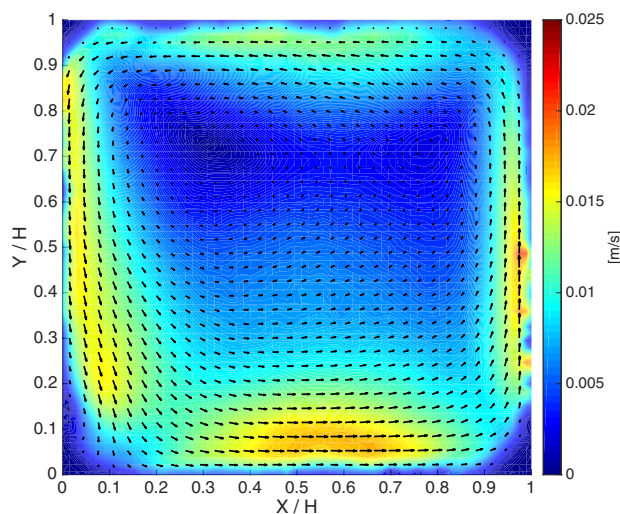


Fig. 9 Time-averaged velocity field of the PIV experiment SC_{gas} . The color scale indicates the magnitude of the mean velocity \bar{u} , while the arrows show its direction. Only one arrow every four data points is plotted

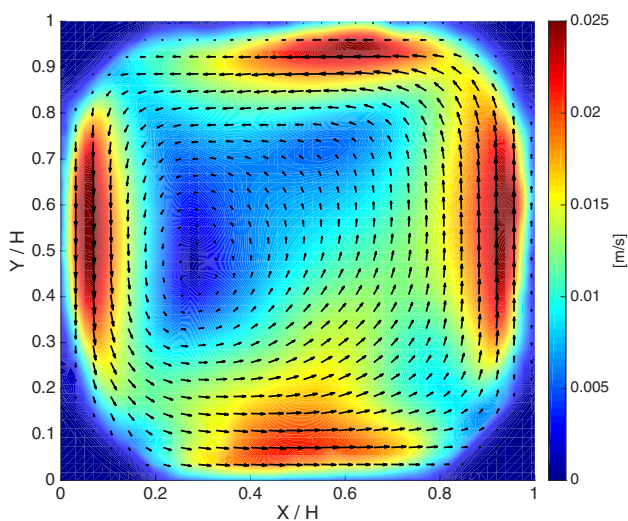


Fig. 8 Time-averaged velocity field of the PIV experiment $SC_{max.4p}$. The color scale indicates the magnitude of the mean velocity \bar{u} , while the arrows show its direction. Only one arrow every four data points is plotted

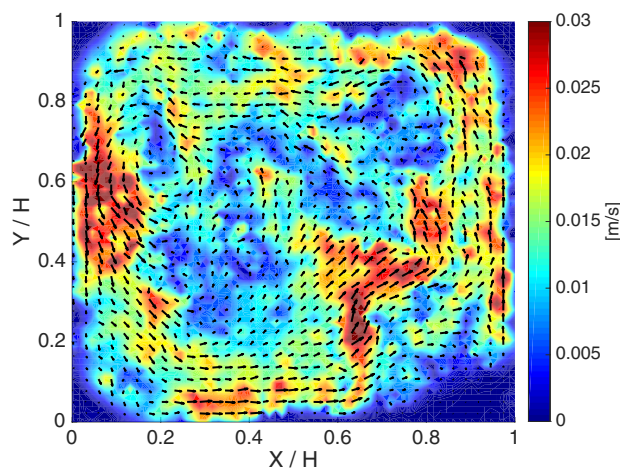


Fig. 10 Instantaneous velocity field of the PIV experiment SC_{liquid} . The color scale indicates the magnitude of the instantaneous velocity u_i , while the arrows show its direction. Only one arrow every four data points is plotted

not introduce a bias error in the mean flow field, as explained in Sect. 3.2.

4.3 PIV uncertainty from correlation statistics

The uncertainty on the instantaneous velocity was estimated *a posteriori*, using the method developed by Wieneke (2015). This instantaneous uncertainty estimate includes contributions from optical distortions, e.g., blurring, low

image seeding density and strong spatial gradients in particle displacement. The estimation method needs as inputs instantaneous velocity vector fields and their two corresponding camera images. Based on the measured velocity field, the two camera images are dewarped to the same time instant halfway in between the interval between the recordings. If there was no uncertainty in the measurements, the two dewarped frames should overlap perfectly. This part of the method is similar to the image matching method proposed by Sciacchitano et al. (2013). Wieneke’s method then focuses on the asymmetry in the peak of the

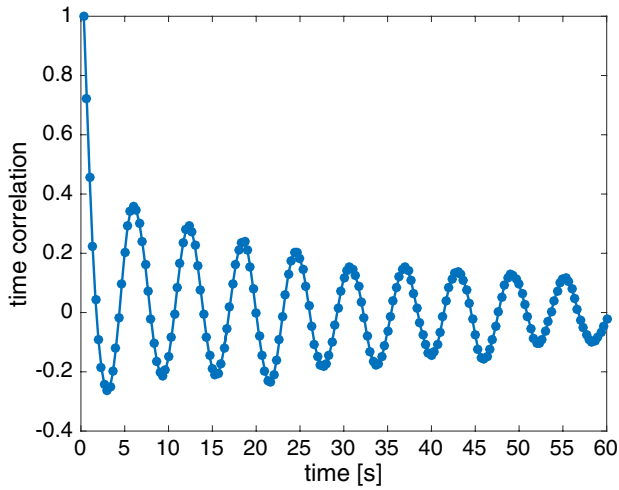


Fig. 11 Time correlation of the velocity in a rectangular region of 10×15 data points centered at $X/H \approx 0.9$ and $Y/H \approx 0.5$, for the experiment SC_{liquid}

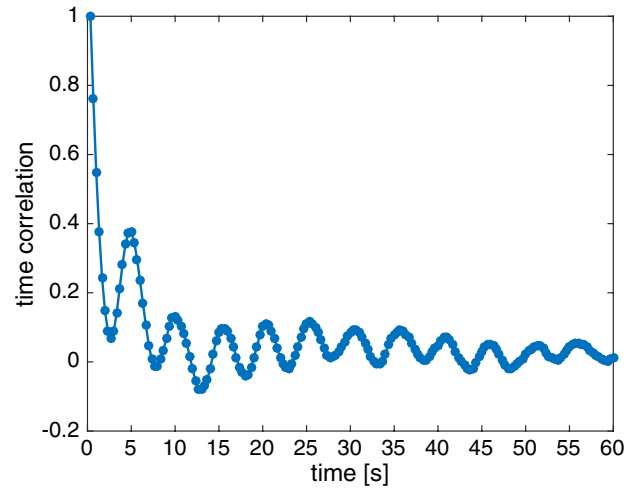


Fig. 12 Time correlation of the velocity in a rectangular region of 10×15 data points centered at $X/H \approx 0.9$ and $Y/H \approx 0.5$, for the experiment $SC_{\text{max } \Delta \rho}$

cross-correlation function between the two dewarped images, and considers the individual pixels contributions to the cross-correlation peaks. It is appropriate in the present case, especially because it allows to take into account the effect of optical distortions as deformed particle image shapes in one or both frames. This may lead to asymmetric cross-correlation peaks. Figure 14 shows the velocity uncertainty for the instantaneous velocity field of Fig. 10, computed as in Wieneke (2015). Only the points where the estimated uncertainty value is smaller than one pixel were considered reliable. This corresponds to about 75% of the measurement section. In the reliable region the average uncertainty was ≈ 0.53 pixels displacement. This value corresponds to $\approx 5, 7\%, \approx 5.7\%$, and $\approx 10\%$ of the average large scale circulation velocity, as determined in Sect. 4.2, for the experiments $SC_{\text{liquid}}, SC_{\text{max } \Delta \rho}$, and SC_{gas} , respectively. Comparing the instantaneous velocity field of Fig. 10 and its statistical uncertainty shown in Fig. 14, it can be observed that in the bottom part of Fig. 14, at $X/H \approx 0.6$, there is a large region extending vertically and bending towards the right, with large uncertainties, which corresponds to strong upward plume in Fig. 10. Visual inspection revealed a locally strong non-uniform particle displacement suggesting fine scale flow structures that could not be resolved. This implies that the values of the integral velocity scale of the flow could be measured reliably, but smaller scales could not.

5 Summary

PIV measurements of a supercritical fluid in RB convection were presented to investigate the feasibility of PIV in fluids with severe optical distortions. The experimental conditions

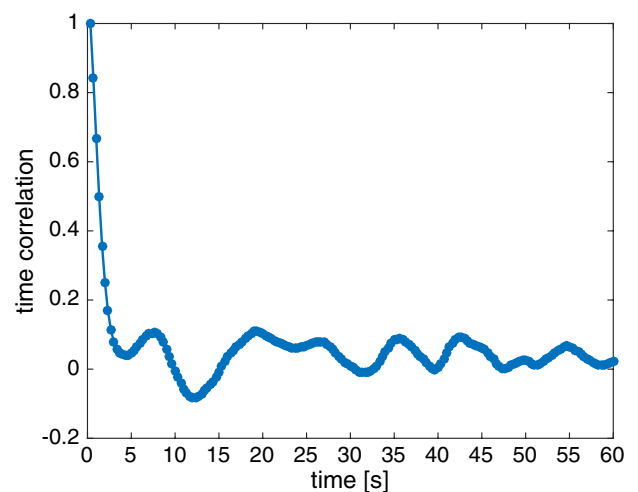


Fig. 13 Time correlation of the velocity in a rectangular region of 5×15 data points centered at $X/H \approx 0.9$ and $Y/H \approx 0.5$, for the experiment SC_{gas}

Table 4 Large-scale circulation velocity, U_{LSC} , statistical relative uncertainty, $\delta u(\tau)$, standard deviation (σ_u), and characteristic time τ , in the PIV experiments $SC_{\text{liquid}}, SC_{\text{max } \Delta \rho}$ and SC_{gas} , computed in a region of 10×15 data points centered in $X/H \approx 0.9$ and $Y/H \approx 0.5$

	PIV SC_{liquid}	PIV $SC_{\text{max } \Delta \rho}$	PIV SC_{gas}
U_{LSC} [mm/s]	20.6	19.4	11.8
$\delta u(\tau)$	1%	1%	1.1%
σ_u [mm/s]	5.11	4.08	3.2
τ [s]	5.3	6	10

were chosen to study different parts of the ρ versus T curve at constant pressure. Three cases were studied with a maximum

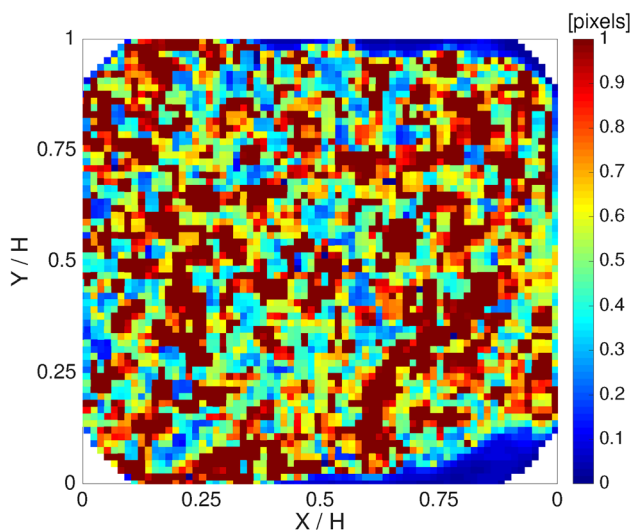


Fig. 14 Estimation of the velocity uncertainty, for the SC_{liquid} PIV instantaneous measurement of Fig. 10

relative density difference within the cell, between 17% and 42%.

A preliminary BOS study was performed to quantify the effects of strong density changes within the flow, which lead to strong optical distortions. It was found that for the present experimental conditions, blurring due to optical distortions did not obstruct the visualization of the particles, except in the boundary layer regions. From the spatial gradient of instantaneous BOS displacements, an upper bound for the PIV velocity error due to optical distortions was estimated at approximately 5%.

Appropriate tracers particles were selected to accurately follow the flow according to criteria proposed by Mei (1996). The uncertainty in the measured velocity related to errors in the PIV cross-correlation associated with image blurring and particle deformation, was estimated with Wieneke's method (Wieneke 2015). The velocity was accurately measured, with uncertainty within 10%, in approximately 75% of the measurement section. This allowed us to conclude that with strong density changes, it was possible to reliably measure the integral velocity of the flow, while smaller scales could not be resolved. The time-averaged velocity fields showed the presence of a large-scale circulation roll for all three cases. This large-scale flow structure is typical of RB convection (Ahlers et al. 2009). The results showed strong asymmetries that can be explained by the strong temperature dependency of the fluid properties.

Acknowledgements The authors would like to acknowledge the technicians who worked on the construction and the commissioning tests of the experimental facility: Ing. Dick de Haas, Ing. Peter van der Baan, and Ing. John Vlieland. This research is supported by the Dutch Technology Foundation STW, which is part of the Netherlands Organization

for Scientific Research (NWO), and which is partly funded by the Ministry of Economic Affairs.

References

- Adrian RJ, Westerweel J (2011) Particle image velocimetry. Cambridge aerospace series. Cambridge University Press, Cambridge
- Ahlers G, Grossmann S, Lohse D (2009) Heat transfer and large scale dynamics in turbulent Rayleigh-Bénard convection. *Rev Mod Phys* 81(2):503
- American Society of Heating R, Engineers AC (2017). <https://www.ashrae.org>. <https://www.ashrae.org>
- Ashkenazi S, Steinberg V (1999) High Rayleigh Number Turbulent Convection in a Gas near the Gas-Liquid Critical Point. *Phys Rev Lett* 83(18):3641–3644
- Avdeev MV, Konovalov AN, Bagratashvili VN, Popov VK, Tsykina SI, Sokolova M, Ke J, Poliakov M (2004) The fibre optic reflectometer: a new and simple probe for refractive index and phase separation measurements in gases, liquids and supercritical fluids. *Phys Chem Chem Phys* 6:1258–1263
- Bell IH, Wronski J, Quoilin S, Lemort V (2014) Pure and pseudo-pure fluid thermophysical property evaluation and the open-source thermophysical property library coolprop. *Indus Eng Chem Res* 53(6):2498–2508
- Boussinesq J (1903) *Théorie analytique de la chaleur*, vol 2. Gauthier-Villars, Paris
- Buongiorno J, MacDonald PE (2003) Supercritical water reactor (scwr) progress Report for the FY-03 Generation-iv R&D Activities for the Development of the SCWR in the U.S. Tech. rep., INEEL
- Elsinga GE, Orlicz GC (2015) Particle imaging through planar shock waves and associated velocimetry errors. *Exp Fluids* 56:129. <https://doi.org/10.1007/s00348-015-2004-9>
- Elsinga GE, van Oudheusden BW, Scarano F (2005) Evaluation of aero-optical distortion effects in PIV. *Exp Fluids* 39:246–256
- Fehrer EG (1968) The supercritical thermodynamic power cycle. *Energy Convers* 8(2):85–90
- International Forum GIF (2017). https://www.gen-4.org/gif/jcms/c_9260/public
- Horn S, Shishkina O (2014) Rotating non-Oberbeck-Boussinesq Rayleigh-Bénard convection in water. *Phys Fluids* 26(5):055,111
- Horn S, Shishkina O, Wagner C (2013) On non-Oberbeck-Boussinesq effects in three-dimensional Rayleigh-Bénard convection in glycerol. *J Fluid Mech* 724:175–202
- Huang D, Wub Z, Sunden B, Li W (2016) A brief review on convection heat transfer of fluids at supercritical pressures in tubes and the recent progress. *Appl Energy* 162:494–505
- Jackson J (2006) Studies of buoyancy-influenced turbulent flow and heat transfer in vertical passages. In: *Proceedings of the annals of the assembly for international heat transfer conference 13*. <https://doi.org/10.1615/IHTC13.p30.240>
- Jackson J (2013) Fluid flow and convective heat transfer to fluids at supercritical pressure. *Nucl Eng Design* 264:24–40
- Jiang P, Shi R, Xu Y, He S, Jackson J (2006) Experimental investigation of flow resistance and convection heat transfer to CO_2 at supercritical pressures in a vertical porous tube. *J Supercr Fluids* 38(3):339–346
- Karellas S, Schuster A (2008) Supercritical fluid parameters in organic rankine cycle applications. *Int J Thermodyn* 11(3):101–108
- Kurganov VA, Kaptil'ny AG (1992) Velocity and enthalpy fields and eddy diffusivities in a heated supercritical fluid flow. *Exp Thermal Fluid Sci* 5:465–478
- Lemmon E, Huber M, McLinden M (2013) NIST reference database 23: reference fluid thermodynamic and transport properties-REFPROP, version 9.1. Standard Reference Data Program

- Licht J, Anderson M, Corradini M (2009) Characteristics in supercritical pressure water. *J Heat Transfer* 131:072502
- Mei R (1994) Flow due to an oscillating sphere and an expression for unsteady drag on the sphere at finite Reynolds number. *J Fluid Mech* 270:133–174
- Mei R (1996) Velocity fidelity of flow tracer particles. *Exp Fluids* 22:1–13
- Melling A (1997) Tracer particles and seeding for particle image velocimetry. *Measure Sci Technol* 8(12):1406
- Murphy MJ, Adrian RJ (2010) PIV space-time resolution of flow behind blast waves. *Exp Fluids* 49(1):193–202. <https://doi.org/10.1007/s00348-010-0843-y>
- Oka Y, Koshizuka SI (1993) Concept and design of a supercritical-pressure, direct-cycle light water reactor. *Nucl Technol* 103(3):295–302
- Pioro I (2013) Nuclear power as a basis for future electricity production in the world: generation III and IV reactors (Chapter 10). In: Mesquita A (ed) *Current research in nuclear reactor technology in Brazil and Worldwide*. IntechOpen. <https://doi.org/10.5772/56032>
- Pioro I, Kirillov P (2013) Current status of electricity generation in the world, vol *Materials and processes for energy: communicating current research and technological developments*. A. Méndez-Vilas
- Pioro IL, Romney B (2016) *Handbook of generation iv nuclear reactors*. Woodhead publishing series in energy. Woodhead Publishing, Sawston
- Pioro IL, Khartabil HF, Duffey RB (2004) Heat transfer to supercritical fluids flowing in channels—empirical correlations (survey). *Nucl Eng Design* 230:69–91
- Raffel M, Willert C, Wereley S, Kompenhans J (2007) *Particle image velocimetry*, 2nd edn. Springer-Verlag, Berlin Heidelberg
- Richard H, Raffel M (2001) Principle and applications of the background oriented schlieren (BOS) method. *Measure Sci Technol* 12:1576–1585
- Schuster A, Karellas S, Aumann R (2010) Efficiency optimization potential in supercritical Organic Rankine Cycles. *Energy* 35:1033–1039
- Sciacchitano A, Wieneke B, Scarano F (2013) PIV uncertainty quantification by image matching. *Measure Sci Technol* 24:045302
- Valori V (2018) *Rayleigh-Bénard convection of a supercritical fluid: PIV and heat transfer study*. PhD thesis, Delft University of Technology
- Valori V, Elsinga G, Rohde M, Tummers M, Westerweel J, van der Hagen T (2017) Experimental velocity study of non-Boussinesq Rayleigh-Bénard convection. *Phys Rev E* 95(053):113
- Vukoslavčević P, Radulović I, Wallace J (2005) Testing of a hot- and cold-wire probe to measure simultaneously the speed and temperature in supercritical CO₂ flow. *Exp Fluids* 39(4):703–711
- Wieneke B (2015) PIV uncertainty quantification from correlation statistics. *Measure Sci Technol* 26:074002
- Yoo JY (2013) The turbulent flows of supercritical fluids with heat transfer. *Annu Rev Fluid Mech* 45:495–525

Publisher's Note Springer Nature remains neutral with regard to jurisdictional claims in published maps and institutional affiliations.

Affiliations

Valentina Valori^{1,2,3}  · Gerrit E. Elsinga² · Martin Rohde¹ · Jerry Westerweel² · Tim H. J. J. van der Hagen¹

✉ Valentina Valori
valentina.valori@cea.fr

Gerrit E. Elsinga
g.e.elsinga@tudelft.nl

Martin Rohde
m.rohde@tudelft.nl

² Laboratory for Aero and Hydrodynamics, Faculty of Mechanical, Maritime and Materials Engineering, Delft University of Technology, Mekelweg 2, 2628 CD Delft, The Netherlands

³ Present Address: DSM/IRAMIS/SPEC, CNRS UMR 3680, CEA, Univ. Paris-Saclay, 91191 Gif-sur-Yvette, France

¹ Radiation Science and Technology Department, Faculty of Applied Sciences, Delft University of Technology, Mekelweg 15, 2629 JB Delft, The Netherlands